Supporting Information

Superhydrophobic-oleophobic Ag Nanowire Platform: An Analyte-concentrating and Quantitative Aqueous and Organic Toxin SERS Sensor

Xing Li,[†,+] Hiang Kwee Lee,[†, ‡,+] In Yee Phang,[‡] Choon Keong Lee,[†] Xing Yi Ling[†,*]

† Division of Chemistry and Biological Chemistry, School of Physical and Mathematical Sciences, Nanyang Technological University, 50 Nanyang Ave, Singapore 637371

‡ Institute of Materials Research and Engineering, A*STAR (Agency for Science, Technology and Research), 3 Research Link, Singapore 117602

[+] These authors contributed equally to this work.
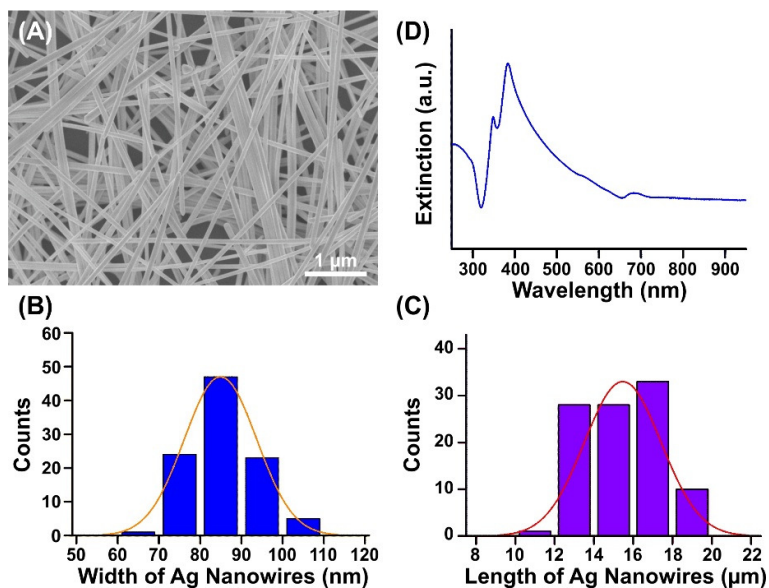
* E-mail: xyling@ntu.edu.sg

Figure S1. Characterizations of as-synthesized Ag nanowires. (A) SEM image of Ag nanowires. (B) Width and (C) length distributions of Ag nanowire. (D) UV-vis spectra of Ag nanowires.

The as-synthesized Ag nanowires exhibits characteristic localized surface plasmon resonances at 349 and 384 nm, which are assigned to the transverse modes of Ag nanowires out-of-plane quadrupole resonance and out-of-plane resonance, respectively.[1]
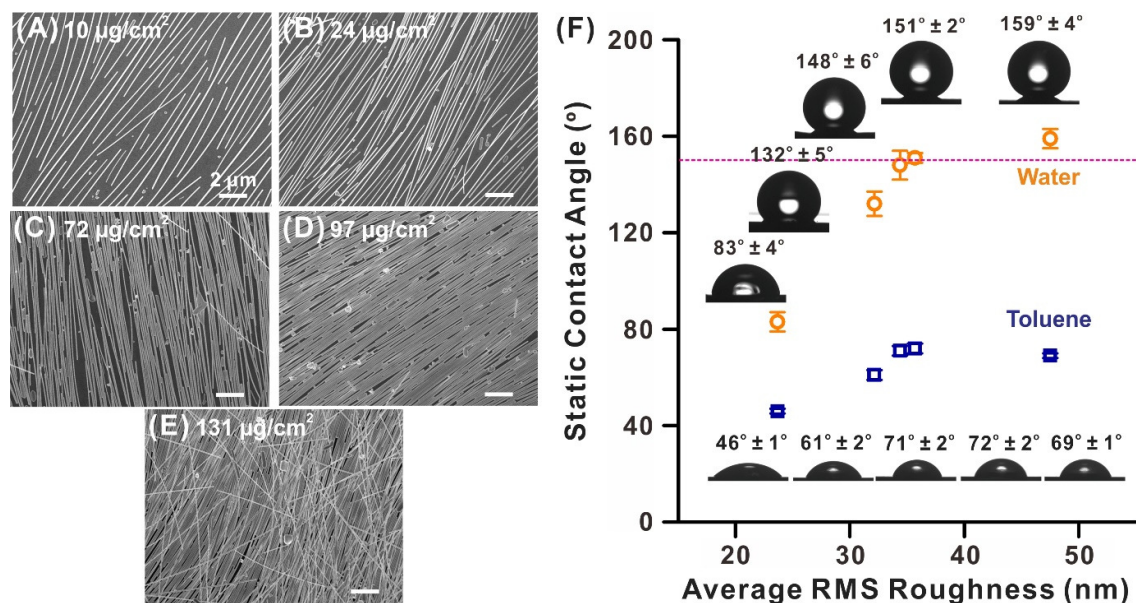
Figure S2. Effect of Ag nanowire surface densities applied during Langmuir-Schaefer monolayer assemblies on anti-wetting properties. (A - E) SEM images of Ag nanowire monolayers fabricated using surface density of 10, 24, 72, 97 and 131 $\mu g/cm^2$ respectively. (F) Static contact angles of water and toluene as a function of surface roughness, which correspond to Ag nanowire surface density of 10, 24, 72, 97 and 131 $\mu g/cm^2$ (from left to right). Purple dotted line denotes super-phobicity ($\geq 150^o$).

We systematically vary the Ag nanowire surface density applied during Langmuir-Schaefer monolayer assemblies to study the effect of surface roughness on latter anti-wetting properties. Using a low Ag nanowire surface density of 10 $\mu g/cm^2$ (Figure S2A), the as-fabricated Ag nanowire monolayer is observed to be direction-oriented and sparsely distributed. As the Ag nanowire surface density increases to eventually 97 $\mu g/cm^2$ (Figure S2B – D), we observe that the assembled monolayers become more compact and aligned. However, upon further increment of Ag nanowires to 131 $\mu g/cm^2$ (Figure S2E), multilayer of randomly-oriented Ag nanowire is observed. We will also like to emphasize that Ag nanowire surface density less than 10 $\mu g/cm^2$ and over 131 $\mu g/cm^2$ are not studied, as the former forms sparse Ag nanowires insufficient for creating a rough surface for anti-wetting properties while the latter results in uncontrollable multi-layer aggregation of randomly-oriented Ag nanowires.

The root-mean-square (RMS) roughness is then measured using atomic force microscopy (AFM) to determine the effect of surface asperities on anti-wetting properties (Figure S2F). At Ag nanowire density of 10 μg/cm^2, the as-prepared substrate exhibits a surface roughness of (24 ± 1) nm. Increasing the Ag nanowire surface density from 10 μg/cm^2 to eventually 97 μg/cm^2 leads to an increment of surface roughness from (24 ± 1) nm to (37 ± 11) nm, the maximum surface roughness achievable using a monolayer of Ag nanowire. Hence, it is apparent that Ag nanowire surface density is a viable parameter to tune the compactness of the Ag nanowire monolayer, which ultimately allows surface roughness to be controlled.

Anti-wetting are then rendered to the as-assembled monolayers via grafting of 1*H*,1*H*,2*H*,2*H*-perfluorodecanethiol and subsequently quantified using static contact angles of water and toluene. Correlation of static contact angles with surface roughness reveals a general increment of anti-wetting properties as surface roughness rises from (24 ± 1) nm to (37 ± 11) nm, where water and toluene static contact angles also increases from (83 ± 4)^o to (151 ± 2)^o and (46 ± 1)^o to (72 ± 2)^o, respectively (Figure S2F). Such observations are in close agreement to Wenzel and Cassie-Baxter theoretical models which state and emphasize the need of high surface roughness and omniphobic surface functionality to achieve anti-wetting properties against water and other liquids.[2] Although superhydrophobicity (water static contact angle ≥ 150°) has been achieved using an Ag nanowire surface density of 97 μg/cm^2, we note that low surface-tension toluene still readily spread across the surface (toluene static contact angle ~ 70°). Hence, we infer that a further increase in surface roughness is necessary for improving the anti-wetting properties of our platform, potentially achievable via systematic and ordered assembly of multi-layer 3D Ag nanowire array. This deduction is further supported by the higher surface roughness of (48 ± 28) nm and static water contact angles of (159 ± 4)^o on a multi-layer Ag nanowire array fabricated using Ag nanowire density of 131 μg/cm^2.
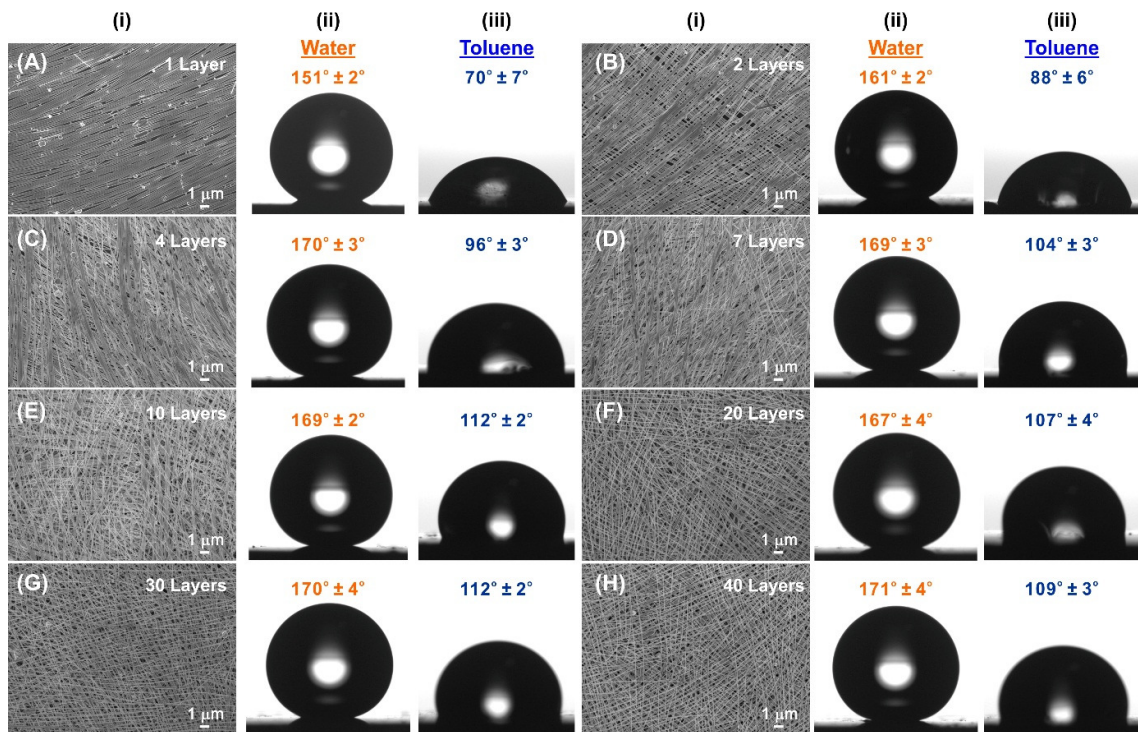
Figure S3. Characterization of 3D Ag nanowire mesh-like arrays fabricated using different layers of Ag nanowire. (A – H) denote 1, 2, 4, 7, 10, 20, 30 and 40 layers of Ag nanowires, respectively. (i) SEM images, (ii) water static contact angles and (iii) toluene static contact angles at respective layers of Ag nanowire.

Based on the SEM images in Figure S3, we determine the inter-particle gaps between adjacent Ag nanowires using ImageJ, a free image analysis software. For an Ag nanowire monolayer, we observe a closely-packed Ag nanowire array with inter-particle gap of ~ 8 nm (Figure 1B, Figure S3A). Upon the assembly of second Ag nanowire layer, an approximate orthogonal-alignment relative to the underlying first layer is observed with a larger inter-particle gap of 46 nm (Figure 1C, Figure S3B). Further increment to 10-layers and eventually 40-layers of Ag nanowires increases and maintains inter-particle distance at ~ 600 nm while the approximate 90° alignment between consecutive layers are still being observed (Figure 1D – E, Figure S3C - H).

Discussion Static Contact Angle and Contact Angle Hysteresis of Water and/or Toluene

The initial scaling of hydrophobicity between 0-layer and 4-layers of Ag nanowires (Figure 1G) agrees well with both theoretical model of superhydrophobicity proposed by Wenzel and Cassie-Baxter, which states that surface roughness is crucial in achieving of superhydrophobic surface.[2] The subsequent plateau of contact angles beyond 4 layers of Ag nanowires can be mainly attributed to the similar apparent surface roughness between 4 to 40 layers and also the gravitational effect on the water droplet that prevents further increase of contact angle to ideal 180° (complete spherical structure).

Typically, a high contact angle hysteresis indicates large extent of liquid/solid adhesion such that liquid droplets readily pin onto the surface. For water, 0 – 4 layers of Ag nanowire have contact angle hysteresis of approximately 34° (Figure 1H). As layers of Ag nanowire increases from 4 to 7 and eventually to 10 layers, contact angle hysteresis decreases to $20^{\circ} \pm 3^{\circ}$ and $12^{\circ} \pm 2^{\circ}$ respectively. Further increment to 40 layers of Ag nanowires leads to constant contact angle hysteresis of about 10°. In contrary, toluene exhibits an initial increment of contact angle hysteresis from $38^{\circ} \pm 2^{\circ}$ to $108^{\circ} \pm 3^{\circ}$ as the layers of Ag nanowires increase from 0 to 10 layers and subsequently plateau at approximately 107° even upon further increments of Ag nanowire layer. The contact angle hysteresis plateaus for all liquids agree well with previous discussion, where relatively constant surface roughness and liquid static contact angles are also observed between 10 – 40 layers of Ag nanowires. The contrasting phenomenon of water and toluene contact angle hysteresis is mainly attributed to the large differences in surface tension. Water, with high surface tension, has strong cohesive force which enables the Cassie-Baxter-like behavior to be achieved readily,[3-4] where the droplets stay mainly on top of the Ag nanowire asperities. Hence, minimal liquid-solid interaction occurs and leads to low adhesion of water droplet to the superhydrophobic surface. On the other hand, toluene has a lower surface tension which make it wet the surface asperities easily (Wenzel-like), increasing both liquid-solid interfacial area and adhesion within the confined droplet area.[5]
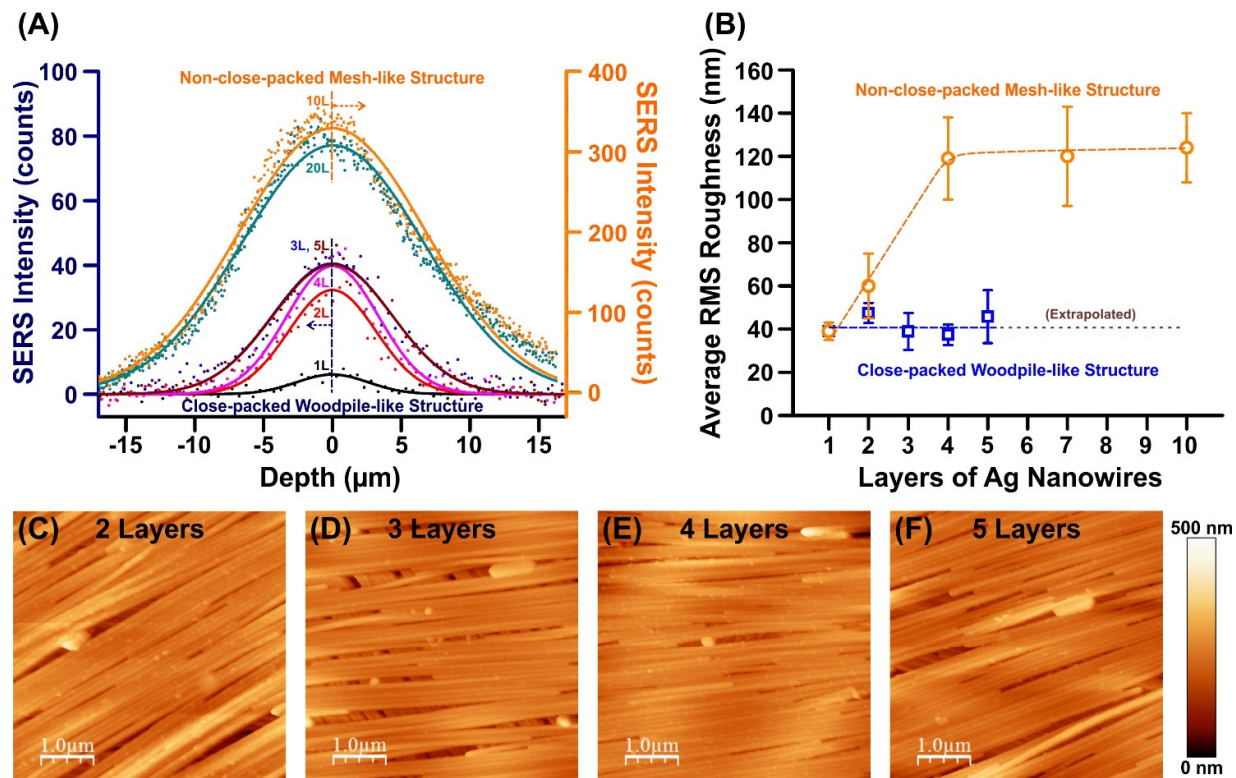
Figure S4. Comparison of non-close-packed mesh-like structure with close-packed woodpile-like structure. (A) SERS intensity as a function of z-distance and (B) surface roughness as a function of Ag nanowire layers of non-close-packed mesh-like structure and close-packed woodpile-like structure. (C – F) AFM images of close-packed woodpile-like structure with 2 - 5 layers of Ag nanowire, respectively.

To demonstrate the superiority of our non-close-packed mesh-like array over closely-packed woodpile-like structures, we systematically compare the surface roughness and laser permeability between these two distinct designs. We first functionalize the Ag surface with a self-assembled monolayer of 4-methylbenzenethiol and compare the laser penetration in non-close-packed and closely-packed Ag nanowire arrays. For woodpile-like structure, we observe that the full-width-half-maximum (FWHM) of intensity-distance profiles increases from 6.2 to 10.2 μm between 1-layer to 3-layers of Ag nanowire and subsequently remained relatively constant at 10.2 μm beyond the 3rd layer (Figure S4A). Hence, the maximum laser permeability of woodpile-like structure is determined to be 3 layers, which is in close agreement to our previous work.[1] On the other hand, our non-close-packed mesh-like structure exhibits a significantly larger FWHM of approximately 15.8 μm for both

10-layers and 20-layers of Ag nanowires, clearly demonstrating the superior laser permeability of our non-close-packed mesh-like Ag nanowire array over woodpile-like structures. Such improved laser permeability in our non-close-packed mesh-like structure is important to access a higher density of "hot spots" for greater SERS enhancement, as observed from the 8-fold increment of maximum SERS intensity between the mesh-like structure (~ 320 counts) and woodpile-like structure (~ 40 counts).

Our non-close-packed mesh-like structure also demonstrates surface roughness at least 3-fold superior than woodpile-like structures at the 10th layer of Ag nanowire (Figure S4B). For non-close-packed mesh-like structure, we observe an initial increment of surface roughness from (39 ± 4) nm to (124 ± 16) nm when the layer of Ag nanowires increases from 1 to 10 layers, respectively, and subsequently plateau beyond the 10th layer at approximately 139 nm. In contrary, woodpile-like structures exhibit similar surface roughness of approximately 40 nm, even with the increase of Ag nanowires from 1 to 4 layers. By extrapolating the surface roughness-Ag nanowire layers plot to the 10th layer, the surface roughness of woodpile-like structure is expected to remain constant at 40 nm, illustrating that the surface roughness arise only from the topmost closely-packed Ag nanowire layer while the underlying layers are mainly unexposed (Figure S4C - F). Hence, the necessity of our non-close-packed Ag nanowire mesh-like array to achieve high surface roughness essential for anti-wetting properties and also enhanced laser permeability over woodpile-like structure is clearly evident.
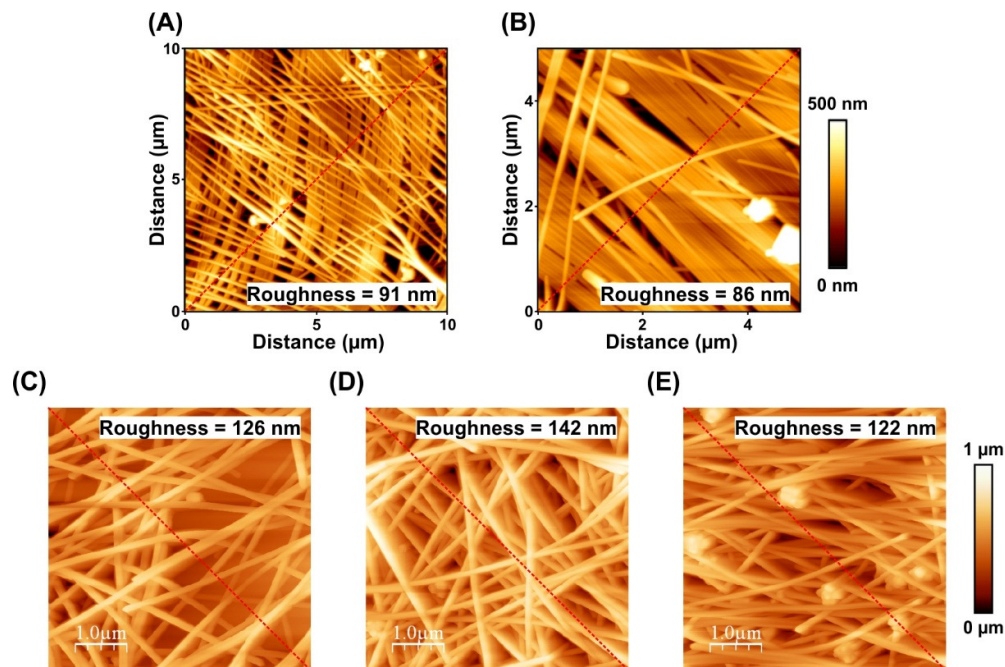
Figure S5. AFM images of 3D Ag nanowire arrays fabricated using different orientation, compactness and/or method. (A) Non-close-packed structure with approximately 90° alignment (orthogonally-aligned) between consecutive Ag nanowire layers. (B) Close packing of Ag nanowires with approximately 0° alignment (parallel-aligned) between consecutive layers. (C - E) Ag nanowire structures fabricated via drop-casting of 19, 85, and 137 μg of Ag nanowires respectively. Red dotted lines denote the profiles where surface roughness are measured.

We systematically study the effect of orientation and compactness of Ag nanowire layers on the resulting surface roughness of the 4-layers Ag nanowire arrays for the latter fabrication of highly roughened 3D Ag nanowire arrays. To note, (A – B) employ a close-packed Ag nanowire monolayer, assembled using Ag nanowire surface density of 97 μg/cm^2 (as discussed in Figure S2), as the base layer. In addition, a sparse Ag nanowire assembly at 0° alignment is not explored due to the difficulties in distinguishing the second layer from the first layer of Ag nanowires. A non-close-packed structure with ~90° alignment between consecutive Ag nanowire layers (A, Figure S5A) exhibits the highest surface roughness of 91 nm. In contrast, a closely-packed Ag nanowire layer, at 0° (B, Figure S5B) alignment, demonstrates lower surface roughness of 86 nm. Such lowering of surface roughness in (B) is potentially due to the masking of the underlying Ag nanowire layer by the top-most compact Ag nanowire layers (also observed in woodpile-like structure, Figure S4),

which in turn reduces the apparent surface roughness. Hence, it is clearly evident that the fabrication of non-close-packed 3D Ag nanowire mesh-like is essential to generate high surface roughness for anti-wetting properties.

We also compare our 3D Ag nanowire mesh-like arrays with Ag nanowire structures fabricated via drop-casting to demonstrate the superiority of our layer-by-layered Langmuir-Schaefer assembly. Generally, all the Ag nanowire structures fabricated via drop-casting demonstrate higher surface roughness of > 120 nm (Figure S5C – E). Despite the higher surface roughness, we will like to emphasize that these Ag nanowire structures are largely inhomogeneous, in terms of distribution and orientation of the Ag nanowires, throughout the substrates. As a result, it is reasonable to expect an inhomogeneous distribution of SERS "hot spots" and also generally weaker "hot spots" as the most intense electromagnetic fields are only generated at the intersection between orthogonally-aligned Ag nanowires (refer to Figure S12 for detailed discussion).[1] Thus, the need of layer-by-layered assembly of Ag nanowires into homogeneous 3D mesh-like arrays to generate stronger and uniform "hot-spots" is again demonstrated in these control experiments.
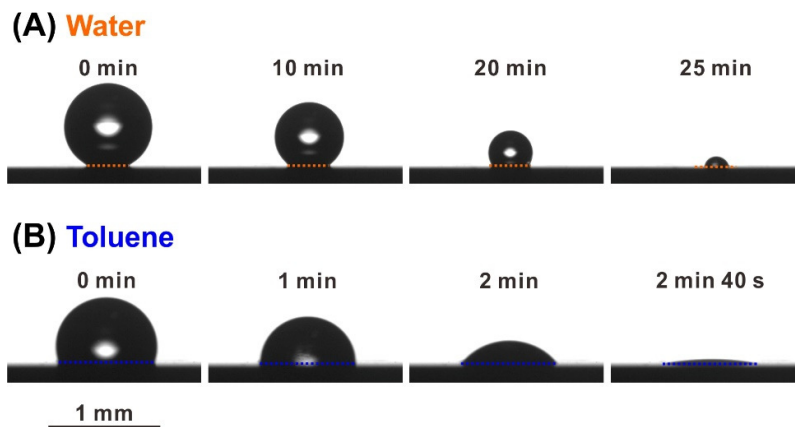
Figure S6. Drying profile of 1-μL (A) water and (B) toluene droplets on superhydrophobic-oleophobic platform. The orange and blue dotted lines denote the initial contact area of the liquid droplets.

We evaporate 1-µL water and toluene droplets on the superhydrophobic-oleophobic platform to determine its effect on the drying behaviour of different liquids (Figure S6). For water, we observe a receding contact area as its volume decreases upon drying. On the other hand, toluene demonstrates strong pinning of the three-phase contact line on the surface such that contact area remains relatively constant even upon complete evaporation at ~ 2 min 40s. These phenomena are due to the low adhesion (lotus-like) of water and high adhesion (rose-petal-like) of toluene on our superhydrophobic-oleophobic platform, as determined using contact angle hysteresis. The differences in drying behaviour therefore further reduces liquid-solid contact area by 2.2 fold for water and remained similar for toluene.
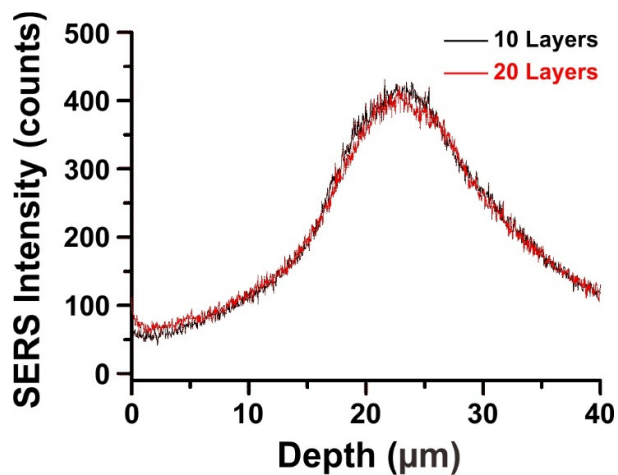
Figure S7. Comparison of laser penetration depth along x-z plane of 10-layers (black) and 20-layers (red) Ag nanowire arrays, using self-assembled monolayer of 4-methylbenzenethiol as probe molecules.

We perform x-z SERS imaging on 4-methylbenzenethiol-grafted 10-layers and 20-layers Ag nanowire arrays to identify any differences in laser penetration depth. Due to the low surface tension of ethanol and complete immersion into large volume of 4-methylbenzenethiol ethanolic solution (~ 5 mL), we assume that the probe molecules can readily access the entire assembly and self-assemble into a monolayer on the surfaces of Ag nanowires. Hence, we neglect the possibility of inhomogeneous distribution of probe molecules on the following discussions. X-z SERS imaging is first scanned using an x-direction focal line at 20 um above the top layer of the Ag nanowire arrays and continue downwards along the z-axis through the use of automated motorized stage. Using the SERS intensity at 1053 cm^{-1} (a combination of phenyl ring-breathing mode, CH in-plane bending and CS stretching), intensity-depth profiles are plotted for both 10-layers and 20-layers Ag nanowire arrays (Figure S7) which appear to overlap each other closely. Hence, these findings strongly suggest that there is no significant differences in the laser penetration depth between 10-layers and 20-layers Ag nanowire arrays.
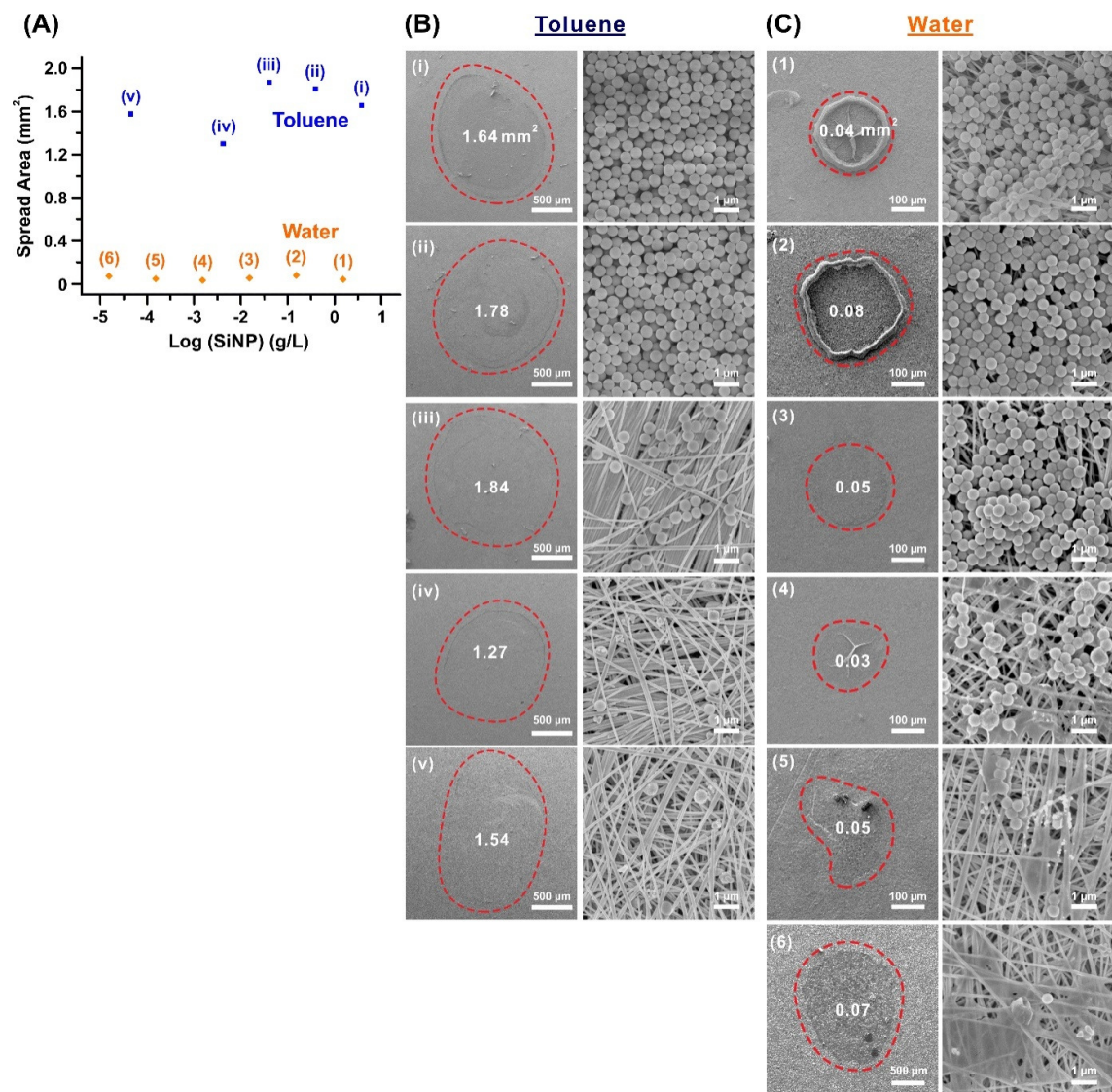
Figure S8. Concentrating effect on superhydrophobic-oleophobic platform using water and toluene. (A) Plot of spread area of dried water and toluene aggregation spots with silica beads concentration. (B) SEM images (at 2 magnifications) of dried aggregation spots of 1-μL toluene solution containing various concentrations of triethoxyoctylsilane-grafted silica beads. (i – v) denotes silica bead concentrations from 4.75 g/L to 4.75×10^{-5} g/L, at 10× dilution interval, respectively. (C) SEM images (at 2 magnifications) of dried aggregation spots of 1-μL water containing various concentrations of silica beads from (1 – 6) 1.53 g/L to 1.53×10^{-5} g/L, at 10× dilution interval, respectively.

Table S1. Characteristic SERS bands of melamine and assignments

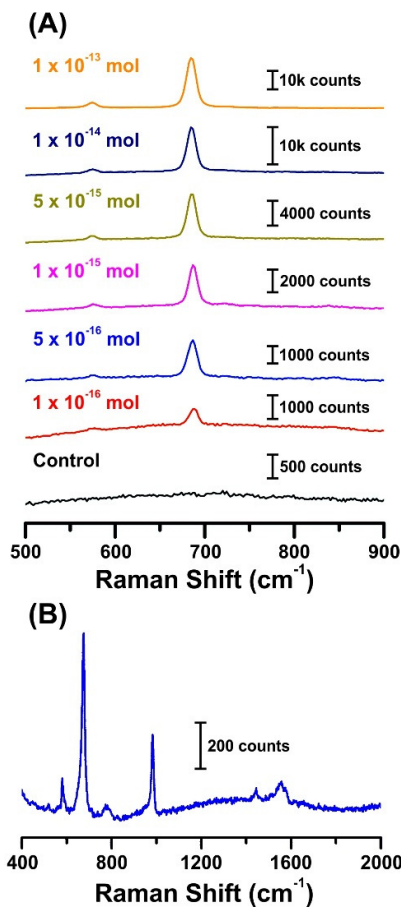| On superhydrophobic-oleophobic SERS platform (cm^{-1})	Band assignment[6-7]
575	NH$_2$ and CNH bending
685	In-plane deformation of triazine ring
979	Ring breathing mode I of triazine ring
1496	Ring and side-chain CN stretching
1554	NCN bending + ring deformation

Figure S9. SERS and Raman characterization of melamine. (A) SERS spectra of melamine at different analyte concentrations on superhydrophobic-oleophobic SERS platform. Control refer to SERS characterization in the absence of melamine. (B) Normal Raman spectrum of solid melamine using laser power and acquisition time of 0.065 mW and 50s respectively.

Analytical enhancement factor (EF) calculation

Analytical enhancement factor (AEF) $= \dfrac{(I_{SERS})/(C_{SERS})}{(I_{Raman})/(C_{Raman})}$

where I_{SERS} and C_{SERS} refer to SERS intensity and concentration of melamine utilized for SERS measurement. I_{Raman} and C_{Raman} denote the normal Raman intensity and concentration of melamine used for normal Raman measurement.

Using density and molecular weight of melamine at 1.57 g/cm^3 and 126.12 g/mol, respectively, we estimate the concentration of solid melamine as followed:

Concentration of solid melamine $= \dfrac{1.57 \times 1000}{126.12} = 12.45$ M

$AEF_{Melamine} = \dfrac{(1040/50)/10^{-10} \text{ M}}{(734/50)/12.45 \text{ M}} = 1.76 \times 10^{11}$

Table S2. Characteristic SERS bands of sudan I and assignments

On superhydrophobic-oleophobic SERS platform (cm^{-1})	Band assignment[8]
465	C=C-N in-plane bending + C=C-C in-plane bending + C-C=O in-plane bending
729	Breathing (naphthyl) + C-C-N + N=N-C + C=C-C in-plane bending (phenyl)
1233	C-H + N-H in-plane bending + N-C1 stretching C=C stretching (naphthyl)
1387	C-N stretching (phenyl + naphthyl) + C=O stretching + C-H in-plane bending
1498	C=C stretching (phenyl) + C-H in-plane bend (phenyl)
1600	C-H in-plane bending (phenyl) + C=C stretch (phenyl) + N-H bending +N=N/C-N stretching

(A)

$$y = \frac{a*b*x}{1 + a*x}$$

(B)

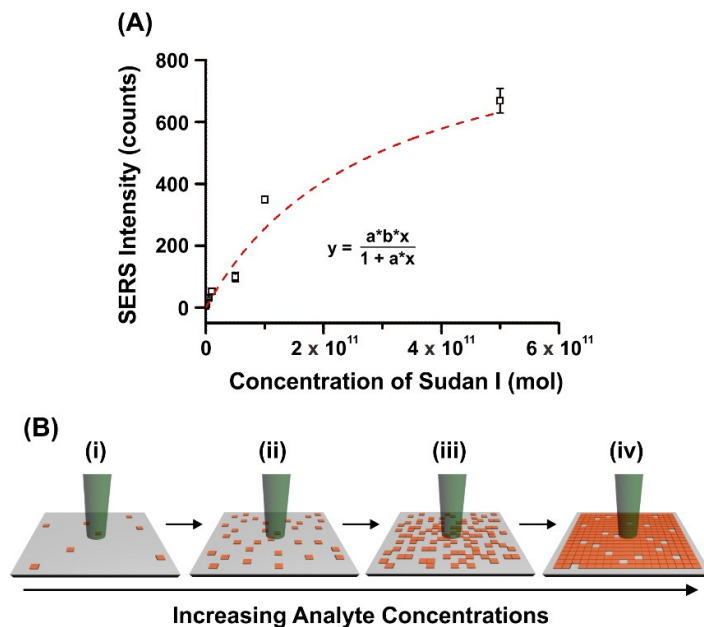**Increasing Analyte Concentrations**

Figure S10. Langmuir adsorption of analytes on superhydrophobic-oleophobic SERS platform. (A) SERS intensities at different sudan I concentrations, fitted using Langmuir-adsorption isotherm (red dotted line). (B) Schematic illustration of the effect of Langmuir adsorption on SERS intensities.

Sudan I is observed to exhibit Langmuir-adsorption behaviour (Figure S10A) on our superhydrophobic-oleophobic SERS platform in the concentration window of interest (0.1 fmol – 50 pmol).[9-10] Using sudan I as an example, the similar SERS intensities (~ 10 counts) for concentration ≤ 0.1 pmol despite the large variation of analyte concentrations is due to the comparable number of analyte molecules within the laser excitation area (Figure S10Bi – ii). As sudan I concentration increases beyond 0.1 pmol, the number of analyte molecules within the laser excitation area increases which leads to the corresponding increment in SERS intensities (Figure S10Bii – iv). Hence, a linearity range is observed from 0.1 pmol to 50 pmol which allows quantitative analysis to be performed.
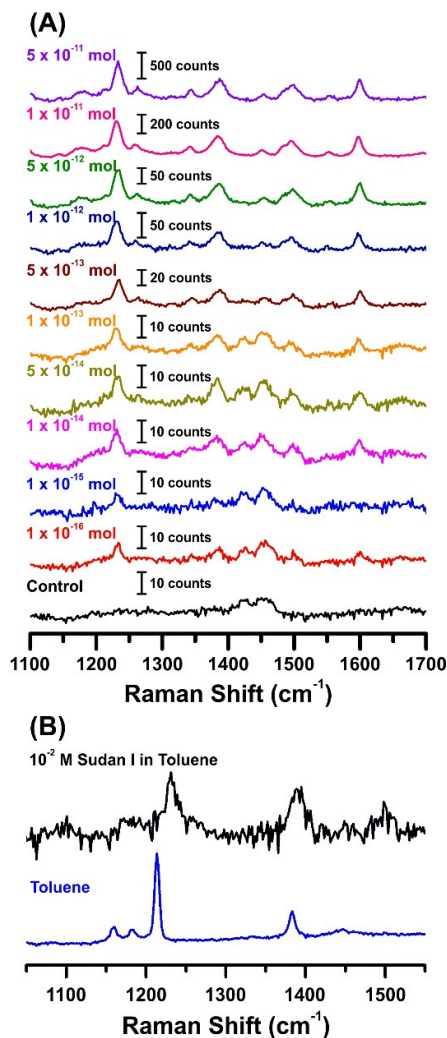
Figure S11. SERS and Raman characterization of sudan I. (A) SERS spectra of sudan I at different analyte concentrations on superhydrophobic-oleophobic SERS platform. Control refer to SERS characterization in the absence of sudan I. (B) Qualitative comparison of normal Raman spectra of sudan I solution (10^{-2} M in toluene) and toluene using laser power and acquisition time of 0.017 mW and 10 s respectively.

Analytical enhancement factor (EF) calculation

$$\text{Analytical enhancement factor (AEF)} = \frac{(I_{SERS})/(C_{SERS})}{(I_{Raman})/(C_{Raman})}$$

where I_{SERS} and C_{SERS} refer to SERS intensity and concentration of sudan I utilized for SERS measurement. I_{Raman} and C_{Raman} denote the normal Raman intensity and concentration of sudan I used for normal Raman measurement.

$$\text{AEF}_{\text{Sudan I}} = \frac{(7.94/10)/10^{-10}}{(4.25/10)/10^{-2}} = 1.87 \times 10^8$$
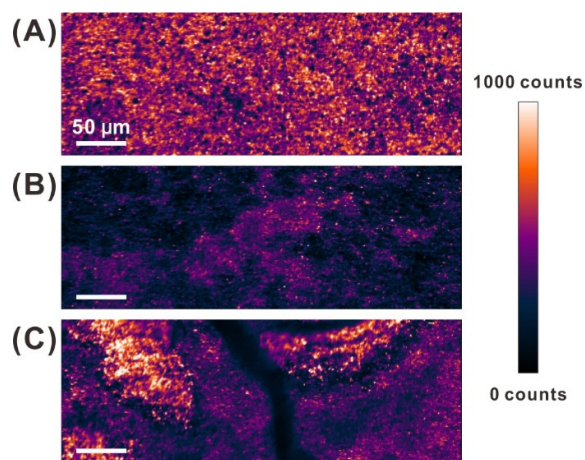
Figure S12. Comparison of SERS-active area between (A) our superhydrophobic-oleophobic SERS platform and Ag nanowire structures fabricated via drop-casting of (B) 19 μg and (C) 85 μg of Ag nanowires. 4-methylbenzenethiol is used as the Raman probe molecule.

We compare the SERS responses of 4-methylbenzenethiol-grafted superhydrophobic-oleophobic SERS platform with the Ag nanowire structures fabricated via drop-casting to re-emphasize the importance of our 3D Ag nanowire mesh-like arrays for large, intense and homogeneous SERS-active area. For our superhydrophobic-oleophobic SERS platform, we observe a large, homogeneous and intense SERS-active areas, extending across 400 × 142 μm along the x- and y-axis respectively (Figure S12A), due to the generation of relatively stronger "hot-spots" only at the intersection of orthogonally-aligned Ag nanowires.[1] In other words, at least 56,000 individual spectrum of intense and consistent SERS responses can be provided by our superhydrophobic-oleophobic SERS platform. On the other hand, both the Ag nanowire structures fabricated via drop-casting exhibit inhomogeneous distributions and generally weaker SERS "hot-spots" (Figure S12B – C) due to the random aggregations and orientations of Ag nanowires (as observed previously in Figure S5C – E). Hence, the need of layer-by-layered assembly of Ag nanowires into homogeneous 3D mesh-like arrays is clearly evident to generate uniform and also intense SERS "hot-spots", which are mainly located at the intersection of orthogonally-aligned Ag nanowires.

References

1. Chen, M.; Phang, I. Y.; Lee, M. R.; Yang, J. K. W.; Ling, X. Y., *Langmuir.* **2013,** *29* (23), 7061-7069.
2. Shirtcliffe, N. J.; McHale, G.; Atherton, S.; Newton, M. I., *Adv. Colloid Interface Sci.* **2010,** *161* (1–2), 124-138.
3. Cassie, A. B. D., *Discuss. Faraday Soc.* **1948,** *3*, 11-16.
4. Cassie, A. B. D.; Baxter, S., *Trans. Faraday Soc.* **1944,** *40*, 546-551.
5. Wenzel, R. N., *J. Phys. Colloid Chem.* **1949,** *53* (9), 1466-1467.
6. Kim, A.; Barcelo, S. J.; Williams, R. S.; Li, Z., *Anal. Chem.* **2012,** *84* (21), 9303-9309.
7. Huang, H.; Shende, C.; Sengupta, A.; Inscore, F.; Brouillette, C.; Smith, W.; Farquharson, S., *J. Raman Spectrosc.* **2012,** *43* (6), 701-705.
8. Kunov-Kruse, A. J.; Kristensen, S. B.; Liu, C.; Berg, R. W., *J. Raman Spectrosc.* **2011,** *42* (6), 1470-1478.
9. Lu, L.-Q.; Zheng, Y.; Qu, W.-G.; Yu, H.-Q.; Xu, A.-W., *J. Mater. Chem.* **2012,** *22* (39), 20986-20990.
10. Lee, H. K.; Lee, Y. H.; Zhang, Q.; Phang, I. Y.; Tan, J. M. R.; Cui, Y.; Ling, X. Y., *ACS Appl. Mater. Interfaces.* **2013,** *5* (21), 11409-11418.
11. Giovannozzi, A. M.; Rolle, F.; Sega, M.; Abete, M. C.; Marchis, D.; Rossi, A. M., *Food Chem.* **2014,** *159* (0), 250-256.